High-throughput search for potential permanent magnet materials

Hanjing Zhou,[1,2,3] Songsong Yan,[1,2] Lin Wu,[1,2] Xiangang Wan [1,2] and Di Wang [1,2,*]

[1]*National Laboratory of Solid State Microstructures and School of Physics, Nanjing University, Nanjing 210093, China*
[2]*Collaborative Innovation Center of Advanced Microstructures, Nanjing University, Nanjing 210093, China*
[3]*International Quantum Academy, Shenzhen 518048, China*

High-performance permanent magnets have a wide range of applications in various fields of the information age. One distinct feature of permanent magnet materials is significant magnetic anisotropy, which is mainly affected by spin-orbit coupling (SOC). Focusing on materials containing 3*d* transition elements with specific Wyckoff positions, where certain partially occupied orbital multiplets can significantly enhance the effect of SOC, we perform a highly efficient search for permanent magnet materials in the inorganic crystal structure database. According to common standards of permanent magnets, we identify 19 potential permanent magnet materials. Among these candidates, 14 materials have already been discussed in previous studies, and we finally propose five new permanent magnet candidates. As examples, the detailed magnetic properties of two candidates among these five new proposed materials are presented. We believe that these potential permanent magnet materials deserve further experimental study.

I. INTRODUCTION

Permanent magnets are widely used in many areas such as transportation, energy, information and communication technology, which are required for the implementation of a large number of technologies, such as electric vehicle motors and generators, windmills, speakers, and relays [1,2]. The main requirements of these materials are large saturation magnetization, high Curie temperature (T_C), and large uniaxial magnetic anisotropy [1,2]. In the past few decades, some representative high-performance permanent magnets materials were discovered and widely used (such as the Nd-Fe-B alloy [3–6], $SmCo_5$ [7,8]). Most of these materials contain rare-earth elements [3,9]. However, there is a growing need to reduce or eliminate the use of rare-earth magnets, which are relatively expensive, by finding rare-earth-free alternatives [1,2]. Therefore, various rare-earth-free permanent magnet materials were proposed recently, including bulk materials [10–13], nanostructure [14–19], and thin films [20–22], but it is still desirable to explore new high-performance permanent magnet materials containing cheaper and less critical elements [1,2].

High-throughput density functional theory (DFT) methods, which can efficiently screen large numbers of compounds, were widely used in past work recently. For example, it has been successfully performed for the discovery of nonmagnetic topological materials and thousands of topological materials candidates were proposed [23–25]. However, the *ab initio* calculation of magnetic topological compounds would be difficult to characterize the ground state when spin-orbit coupling (SOC), which plays an important role in topological properties [26], typically leads to complex magnetic structures. Meanwhile, unlike in nonmagnetic systems, the Coulomb interaction is of substantial importance in most magnetic systems and the Coulomb repulsion is usually incorporated by the parameter U in first-principles calculations [27]. The first-principles predictions for magnetic materials usually depends on the value of U [28,29]. Therefore, compared to the time-reversal-invariant nonmagnetic topological materials, the predictions on magnetic topological materials are relatively few [30]. The same as the case of magnetic topological materials, both the SOC effect and Coulomb interaction are also important for permanent magnetic materials, which makes the efficient search of permanent magnetic materials difficult. At present, people usually perform comprehensive high-throughput DFT methods for rare-earth-free permanent magnetic materials based on their respective screening criteria and range [31–35]. Kusne *et al.* perfomed high-throughput computing and machine learning to search for potential high-performance permanent magnets in Fe-Co-*X* (*X* is the transition-metal element) alloys system and suggested $Fe_{78}Co_{11}Mo_{11}$ to be a rare-earth-free permanent magnet [31]. Meanwhile, Vishina *et al.* presented an application of high-throughput and data-mining approach to predict new permanent magnets containing both 3*d* and 5*d* transition-metal elements based on the Inorganic Crystal Structure Database (ICSD) [36], and the most promising candidates they identified were Pt_2FeNi, Pt_2FeCu, and W_2FeB_2 [32]. Futhermore, they made an extended search for materials containing two different 3*d* elements in the chemical formula and predicted one rare-earth-free permanent magnet candidate Co_3Mn_2Ge finally [33].

Generally, the 3*d* transition metal materials would provide high saturation magnetization and large Curie temperature [32,38], meeting two main requirements of permanent magnets. However, it is commonly believed that SOC does not play an essential role in 3*d* transition metal materials

---

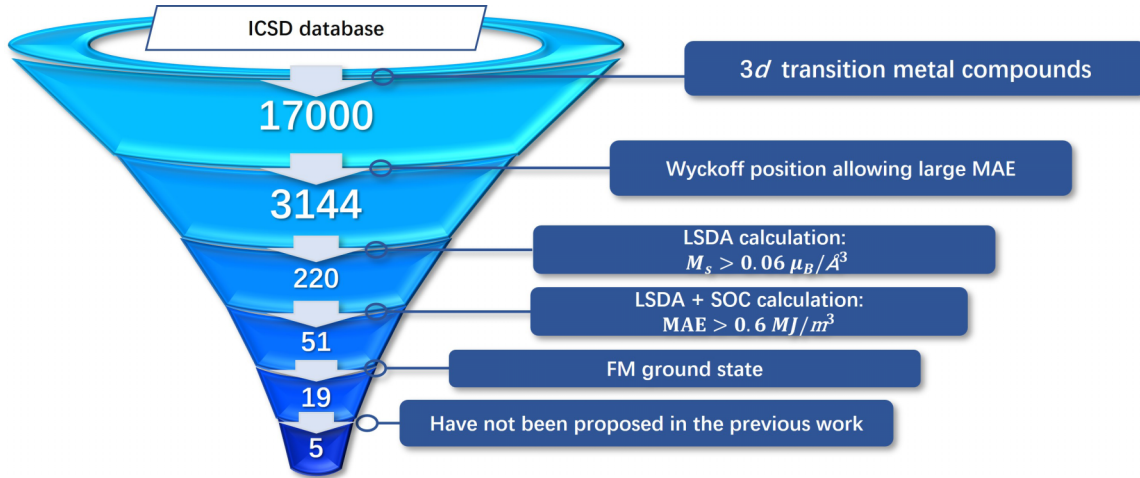*Corresponding author: diwang0214@nju.edu.cn

FIG. 1. Steps of high-throughput search and screening with the number of structures left after each step. In the first step of screening, 17 000 compounds containing $3d$ transition metal elements are selected from the ICSD database. Second, we extract these materials in the corresponding space groups, where the $3d$ transition elements correspond to the specific Wyckoff position allowing large SOC [37]. A total of 3144 different materials are identified. Third, LSDA calculations with FM configuration are performed and 220 materials with the calculated $M_S > 0.06$ $\mu_B/\mathring{A}^3$ are preserved. At the fourth step, LSDA + SOC calculations are performed and 51 candidates meet the filter criteria MAE >0.6 MJ/m^3. Finally, we perform LSDA + SOC (+ U) calculations by considering several different conventional magnetic configurations with different typical magnetic directions to explore their magnetic ground state. Materials with AFM configuration are excluded and 19 FM candidates are left, which are listed in Tables I and VI. Among them, five new candidate materials were not discussed before as candidates of permanent magnets to our best knowledge.

[38,39], resulting in the relatively small magnetic anisotropy energy (MAE). To overcome this shortcoming, the compounds containing both $3d$ and $5d$ transition-metal elements were explored in the previous work [32], which significantly limited the search range of potential permanent magnets materials. It was proposed that, due to certain partially occupied orbital multiplets, the cooperative effect of the electron correlation can significantly enhance the effective SOC in light $3d$ transition metal ions [37]. Therefore, one can screen $3d$ transition metal materials with potentially huge MAEs by simply checking whether the materials belong to the corresponding space groups and whether the $3d$ transition elements occupy the specific Wyckoff positions [37].

In this work, we perform a high-throughput screening for potential permanent magnet materials in ICSD [36]. We focus on $3d$ transition metal materials allowing large SOC according to the certain partially occupied orbital multiplets, and first-principles calculations are then performed to estimate the saturation magnetization, MAE, and magnetic ground state of the screened materials. According to recognized standards of permanent magnets [1,2], we suggest 19 materials to be potential candidates. While 14 materials among them were already discussed in previous studies, we finally obtain five new potential permanent magnets materials FeB$_4$, FeB$_2$, Fe$_2$Sc, Mn$_5$PB$_2$, and Fe$_2$Ge, which are worthy of further experimental investigations. In addition, we present the detailed magnetic properties in two of the new permanent magnet candidates FeB$_4$ and FeB$_2$ as representatives.

II. STEPS OF HIGH-THROUGHPUT SCREENING

As mentioned above, both the SOC effect and Coulomb interaction U play important roles in permanent mag-

nets, which makes it difficult to perform a comprehensive high-throughput first-principles search based on all $3d$ transition metal materials with various magnetic configurations, spin orientations, and different values of the Coulomb parameter U. Here we present a highly efficient search for permanent magnetic materials. This screening is mainly divided into five steps (see Fig. 1) in the following.

(1) During the first step of the material collection stage, we select $3d$ transition metal materials from the ICSD database [36]. As mentioned above, compared to $4d$ and $5d$ elements, $3d$ elements usually provide high saturation magnetization and large Curie temperature [32,38], and the materials containing $4d$ and $5d$ transition elements usually providing magnetism ($4d$: from Nb to Rh, $5d$: from Re to Ir) are excluded. To avoid missing potential materials, we selected all experimental and theoretical materials in the ICSD database. Meanwhile, structures containing rare-earth elements which are expensive were also excluded. There are a total of 17 000 materials after deduplication at the first step.

(2) Second, the $3d$ transition metal materials allowing large MAE are selected. When there are certain partially occupied orbital multiplets in $3d$ materials, the SOC effect could be enhanced by Coulomb correlation [37]. For a d-shell ion exposed to the crystal field, only four types of orbital multiplets are allowed by the crystallographic symmetries, including three doublets E_1 {d_{xz}, d_{yz}}, E_2 {$d_{xy}, d_{x^2-y^2}$}, E_3 {$d_{z^2}, d_{x^2-y^2}$}, and one triplet T {d_{xz}, d_{yz}, d_{xy}} [40]. Among them, the first-order SOC effect is absent in E_3, therefore the magnetic anisotropy for the orbital multiplet E_3 should be small. Meanwhile, in the orbital triplet T {d_{xz}, d_{yz}, d_{xy}}, though the first-order perturbation of the SOC splits the degenerate orbitals, the perturbed energies are independent of the orientation of the magnetization, indicating that the

TABLE I. New proposed materials by screening with desirable properties for permanent magnets. Listed are the material's ICSD, formula, space group, the corresponding 3d translation elements and Wyckoff positions, the calculated MAE (MJ/m³), saturation magnetic moment M_s (μ_B/Å³) and magnetic hardness parameter κ.

ICSD number	Material formula	Space group	Transition elements	Wyckoff positon	MAE (MJ/m³)	M_s (μ_B/Å³)	κ
633 415	Fe_2Sc	194	Fe	2a	0.925	0.0653	1.42
670 859	FeB_4	194	Fe1	2b	2.397	0.0693	2.15
			Fe2	2c			
613 892	FeB_2	191	Fe	1a	5.714	0.0973	2.36
109 111	Mn_5PB_2	140	Mn	1a	0.617	0.1119	0.68
53 460	Fe_2Ge	194	Fe	2a	0.669	0.1219	0.65

first-order SOC effect on the magnetic anisotropy for this orbital triplet T is negligible. Therefore, we select compounds with 3d transition elements corresponding to the specific Wyckoff position allowing E_1 or E_2 orbital multiplets. At this step, about 81.5% of the materials are excluded and 3144 materials are left.

(3) Saturation magnetization (M_S) is one of the most important criteria of the permanent magnet. In this step, we perform local spin-density approximation (LSDA) calculations for the remaining 3144 materials with ferromagnetic (FM) configuration to obtain their M_S. Note that Coulomb interaction usually enhances the magnetic moments in 3d magnetic systems [38,39], therefore, our filter criteria $M_S > 0.06$ μ_B/Å³ [2] from LSDA calculations is strictly to avoid missing potential materials. Meanwhile, SOC usually have little effect on the magnetic moments of 3d magnetic ions [39], thus in this step SOC is also not considered to reduce the computational cost. This screening step leaves about 220 candidates.

(4) In the fourth step, we perform LSDA + SOC calculations with FM configuration to obtain MAE of these potential candidates. Usually one needs to estimate the MAE by performing first-principles calculations with spin orientations along a set of different typical directions. However, for certain partially occupied orbital multiplets in 3d materials [37], the prediction of the easy axis and hard axis of magnetization can be obtained by symmetry analysis. Here we take the degenerate E_1 {d_{xz}, d_{yz}} orbitals in the crystal field as an example, where the SOC interaction could be written as $\lambda L \cdot S$. Since

spin splitting typically overwhelms the SOC effect in 3d systems, we treat SOC as a perturbation with the spin-conserved part only and then the orbital degeneracy is split into states $|l = 2, m = \pm 1\rangle$. When the orbital doublet is half-filled, the occupied state takes the energy of $-\frac{1}{2}\lambda\hbar^2|\cos\theta|$ [41], where θ is the angle between the magnetic moment and the z-axis. The energy of the occupied state is minimized when $\theta = 0$ or π, making out-of-plane magnetization favored. Similarly, the MAE for magnetic materials with half-filled orbital doublet E_2 {$d_{xy}, d_{x^2-y^2}$} is $-\lambda\hbar^2|\cos\theta|$, which also favors the (001) direction to be the easy axis [41]. It is worth mentioning that Coulomb correlation increases the orbital polarization and the effective SOC when the orbital multiplets are partially occupied [37]. With the reinforcement of the orbital polarization and SOC effect, the magnetocrystalline anisotropic energy can significantly increase. Based on LSDA + SOC calculations, the MAE is calculated by the total energy differences between spin orientations along the easy axis and hard axis, and the results of MAE are double-checked by using the force theorem [42,43]. The calculated results based on these two methods are usually similar and we show the ones by energy differences approach if not specified in the following. Note that the Coulomb correlation could further enhance the SOC effect, resulting in a significant gain of the MAE [37]. Therefore, we adopt the appropriate filter criteria to be MAE >0.6 MJ/m³ [2], and in this step 51 materials are left.

(5) Finally, the magnetic structures of these remaining 51 candidates are studied. We perform LSDA + SOC (+U) calculations by considering several different conventional

TABLE II. Relative total energies (E_{tot} in meV/f.u.) of different magnetic ordering states from LSDA (+ U) and LSDA + SOC (+ U) with (001) spin orientation. Here total energy of FM configuration is set to be 0.

	U (eV)	FM	AFM-1	AFM-2	AFM-3	FIM-1
E_{tot}(LSDA)	0.0	0.00	279.54	667.07	457.89	383.41
	0.5	0.00	342.39	663.51	483.29	362.90
	1.0	0.00	368.06	561.34	467.67	309.25
	1.5	0.00	379.13	430.70	470.95	250.38
	2.0	0.00	397.80	368.47	358.63	192.95
E_{tot}(LSDA + SOC)	0.0	0.00	275.61	660.72	456.15	382.36
	0.5	0.00	336.39	632.09	589.25	360.88
	1.0	0.00	359.67	558.92	466.92	308.23
	1.5	0.00	393.34	435.06	482.85	256.38
	2.0	0.00	412.86	385.72	382.36	203.42

TABLE III. Spin exchange parameters (in meV) of FeB_4 evaluated from LSDA ($+ U$) calculations. Meanwhile, the calculated Curie temperature (in K) based on MFT and MC method with different values of U are also summarized in the table.

	Distance (Å)	LSDA	LSDA $+ U$ (= 0.5 eV)	LSDA $+ U$ (= 1.0 eV)	LSDA $+ U$ (= 1.5 eV)	LSDA $+ U$ (= 2.0 eV)
J_1	2.961	−55.59	−52.79	−46.78	−39.25	−29.89
J_2	5.128	−9.31	−15.05	−19.80	−22.54	−21.94
J_3	5.128	−6.23	−5.77	−3.57	−1.86	−1.70
J_4	3.290	−69.88	−85.60	−92.02	−94.78	−99.45
T_C (MFT)		1546	1758	1797	1755	1664
T_C (MC)		945	1186	1217	1227	1126

magnetic configurations with spin orientations along the predicted easy axis to explore their magnetic ground state. Meanwhile, the effect of Coulomb interaction parameter U is also considered. All materials known or suggested to be antiferromagnetic (AFM) are then excluded. Among them, 19 candidates whose magnetic ground states are suggested to be FM remain as potential rare-earth-free permanent magnet materials, which are listed in Tables I and VI and will be discussed in the results section.

III. METHOD

The first-principles calculations were carried out by using the full potential linearized augmented plane-wave method as implemented in the WIEN2K package [44]. The k mesh of the Brillouin zone is set by $60/a$ along each direction, where a denotes the length of the lattice constant in Å. The self-consistent calculations are considered to be converged when the difference in the total energy of the crystal does not exceed 0.01 mRy. We adopt the local spin-density approximation (LSDA) [45] as the exchange-correlation potential and include the SOC using the second-order variational procedure [46]. Meanwhile, the effect of Coulomb repulsion is taken into account by utilizing the LSDA $+ U$ scheme [27].

Monte Carlo (MC) simulations are performed with the METROPOLIS algorithm for the Heisenberg model [47–49]. The size of the cell in the MC simulation in both FeB_4 and FeB_2 are $16 \times 16 \times 16$-unit cells with periodic boundary conditions. At each temperature we carry out 400 000 sweeps to prepare the system and sample averages are accumulated over 800 000 sweeps.

IV. RESULTS

Through our high-throughput search above, we propose 19 candidate materials in the ICSD database that meet the properties of permanent magnets as summarized in Tables I and Appendix. Among these candidates, 14 materials were already discussed in previous studies as potential permanent magnet applications. Some of them were already confirmed by experimental works, such as Fe-Pt alloys [50,51], $Fe_{16}N_2$ [52–55], and Co_5Y [56–58]. We list these known permanent magnet materials in Appendix, and it can be seen that our calculated results are in good agreement with previous works, which also confirms the high efficiency and reliability of our screening method. Finally, to the best of our knowledge, five new candidates are found by our high-throughput calculation and listed in Table I.

As shown in Table I, these five candidates are in three space groups $I4/mcm$ (SG 140), $P6/mmm$ (SG 191), and $P6_3/mmc$ (SG 194). Based on LSDA calculations, their saturation magnetic moments are around 0.06–0.12 $\mu_B/Å^3$, which are larger than one of most famous permanent magnets $Nd_2Fe_{14}B$ (0.04 $\mu_B/Å^3$) [5,6]. Meanwhile, their MAE based on LSDA $+$ SOC calculations are distributed from 0.6 to 5.7 MJ/m^3, where FeB_4 and FeB_2 have the relatively larger MAE (2.4 MJ/m^3 for FeB_4 and 5.7 MJ/m^3 for FeB_2), which has the same order of magnitude as $Nd_2Fe_{14}B$ (4.8 MJ/m^3) [5,6]. Moreover, the magnetic hardness parameter could be evaluated from the expression $\kappa = \sqrt{E_{MAE}/\mu_0 M_s^2}$ and $\kappa > 1$ is an empirical criterion for a material to have a chance of resisting self-demagnetization when made into any possible shape [2]. Their magnetic hardness parameters are distributed from 0.6 to 2.3. According to the screening results, a pair of iron-boron materials (FeB_2 and FeB_4) are included in the candidates. Considering the possible potential of Fe-B alloys as permanent magnet materials, we also extended the calculation of all Fe-B alloys existing in the ICSD database. Their space groups, MAE, and Wyckoff positions occupied by Fe ions are listed in Table VII of the Appendix. In the other Fe-B alloys in the ICSD database, the anisotropy of Fe single ions in these alloys is significantly lower than that of the two screened materials, which also demonstrate the reliability and efficiency of our screening method. It is worth mentioning that FeB_4 comes from theoretical work [59] and warrants further experimental investigations. Besides, there has been experimental work [60] on the magnetic properties of Fe_2Sc, which is suggested to have a large MAE. We will present FeB_4 and FeB_2 in detail and discuss their electronic structure and magnetic properties in the following.

TABLE IV. Relative total energies (E_{tot} in meV/f.u.) of different magnetic ordering states from LSDA ($+ U$) and LSDA $+$ SOC ($+ U$) with (001) spin orientation. Here total energy of FM configuration is set to be 0.

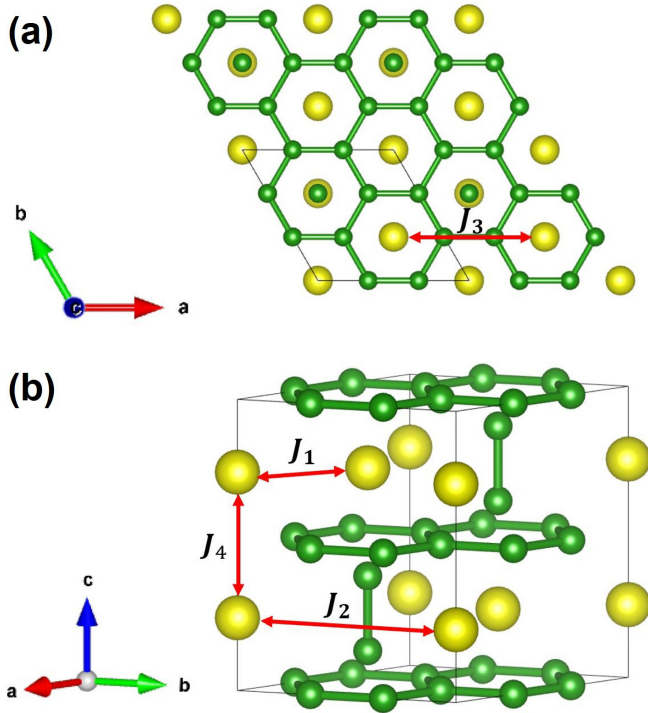|	U (eV)	FM	AFM-1	AFM-2	FIM-1
E_{tot}(LSDA)	0.0	0.00	26.08	57.27	45.14
	0.5	0.00	65.13	93.06	76.07
	1.0	0.00	103.41	127.65	98.61
E_{tot}(LSDA $+$ SOC)	0.0	0.00	23.94	57.12	45.00
	0.5	0.00	61.99	93.41	76.77
	1.0	0.00	99.76	127.05	98.29

FIG. 2. (a). Top view of FeB$_4$. The yellow and green balls represent Fe and B, respectively. (b). The exchange interactions J_1, J_2, J_3, and J_4 are shown. Within (001)-planes, J_1 denote the nearest interactions between Fe1 and Fe2, J_2 denote the nearest interactions between Fe1 ions, J_3 denote the nearest interactions between Fe2 ions. J_4 represent the couplings between two nearest (001)-planes.

A. FeB$_4$

As shown in Fig. 2, FeB$_4$ crystallizes in the hexagonal structure ($P6_3/mmc$, SG 194) [59], where Fe atoms located at two nonequivalent crystallographic sites: Fe1 atoms occupy the $2b$ position: $(0, 0, 1/4)$, and Fe2 atoms occupy the $2c$ position: $(1/3, 2/3, 1/4)$. The site-symmetry group of both Fe ions are all $(-62m)$, which permits the E_1 and E_2 orbital multiplets and is expected to have large MAE.

From LSDA calculations for the FM configuration, FeB$_4$ is suggested to be a metal. The band structure from LSDA calculation is shown in Figs. 3(a) and 3(b), where the main contribution around the Fermi level comes from the $3d$ orbitals of Fe ions. The calculated magnetic moments on the Fe1 and Fe2 sites are 2.66 μ_B and 2.42 μ_B, respectively, indicating $M_S = 0.0693 \, \mu_B/\text{Å}^3$. According to the site symmetry of Fe ions, we perform the LSDA + SOC calculations for (001) and (100) spin directions and estimate the MAE as 2.397 MJ/m^3 with the easy-axis magnetization along the (001) direction as predicted. The band structure from the LSDA + SOC calculation with (001) spin direction is shown in Fig. 3(c). In addition to the energy differences approach, we also calculate the MAE by using the force theorem [42,43] to be about 2.409 MJ/m^3, which is well consistent with the value from energy differences, confirming the reliability of our symmetry analysis and the accuracy of our first-principles calculations. The value of Coulomb parameter U in iron borides was fixed at 0.4 eV in the previous work [61], and we consider the effect of Coulomb interaction with the appropriately wider range of U from 0.0 to 2.0 eV. As shown in Fig. 3(d), the MAE is significantly enhanced by the correlation effect in FeB$_4$ as expected [37].

Finally, to confirm its FM ground state, we consider several different magnetic configurations of FeB$_4$, as shown in Fig. 4. In addition to the FM configuration, we also consider three AFM states and one ferrimagnetic (FIM-1) state: AFM-1, where the Fe atoms couple antiferromagnetically along the c axis; AFM-2, where Fe1 and Fe2 have opposite spin orientations; AFM-3, where both the Fe1 and Fe2 atoms couple antiferromagnetically along the a and b axes; FIM-1 states, where the Fe1 atoms couple ferromagnetically while the Fe2 atoms couple antiferromagnetically along the a and b axes. As shown in Table II, whether SOC is considered, the FM configuration has the lowest total energy with different values of U. Note that SOC has little effect on the calculated energy differences as shown in Table II, and the calculated magnetic moments for the different magnetic configurations are similar (with a difference around than $\pm0.1 \, \mu_B$), allowing us to estimate the Heisenberg exchange couplings by the energy-mapping analysis [62,63] based on LSDA ($+ U$) calculations in the following. As shown in Fig. 2, we consider four magnetic interactions labeled as J_1–J_4 here. The total energies per unit cell for these five spin configurations are
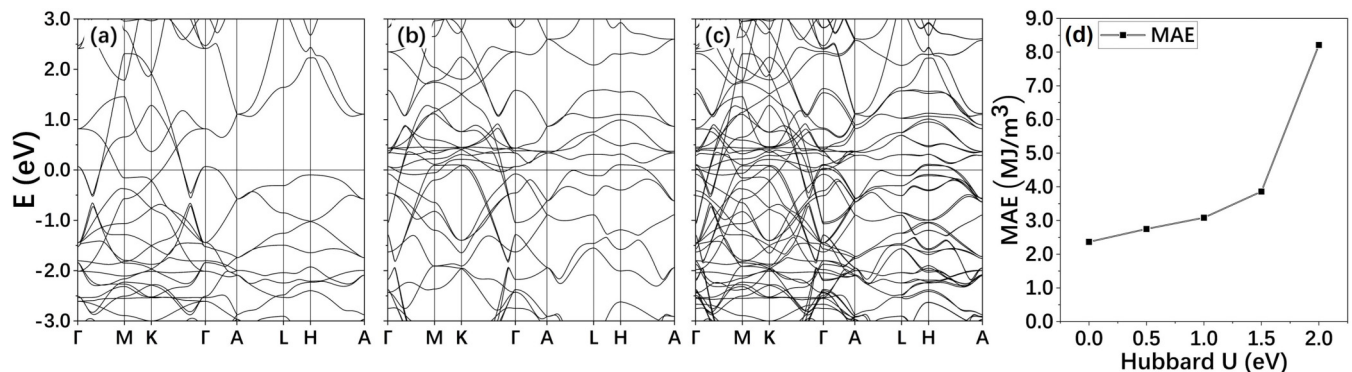

FIG. 3. (a,b) Electronic structure of FeB$_4$ from LSDA calculation with FM configuration for the spin-up and spin-down channels, respectively. (c) Electronic structure of FeB$_4$ from LSDA + SOC calculation with spin orientations along the (001) direction. (d) The calculated MAE value with increasing U.
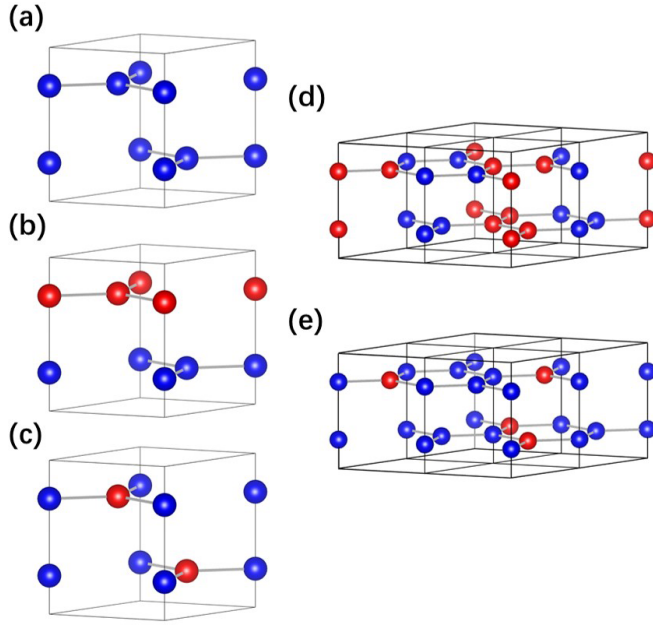
FIG. 4. The magnetic configurations of FeB_4 which we considered in DFT calculations. For clarity only Fe atoms are shown, while the blue and red ones represent Fe ions with up and down spin, respectively. (a)–(e) FM, AFM-1, AFM-2, AFM-3, and FIM-1 configurations, respectively.

expressed as

$$E_{FM} = E_0 + 6J_1 + 6J_2 + 6J_3 + 2J_4,$$
$$E_{AFM-1} = E_0 + 6J_1 + 6J_2 + 6J_3 - 2J_4,$$
$$E_{AFM-2} = E_0 - 6J_1 + 6J_2 + 6J_3 + 2J_4,$$
$$E_{AFM-3} = E_0 - 2J_2 - 2J_3 + 2J_4,$$
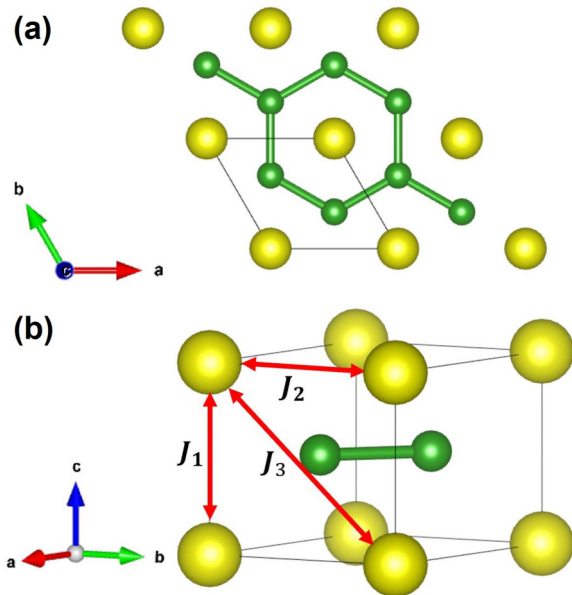$$E_{FIM-1} = E_0 + 6J_2 - 2J_3 + 2J_4. \quad (1)$$

FIG. 5. (a) Top view of FeB_2. The yellow and green balls represent the Fe and B, respectively. (b).The nearest-neighbor, nearest-neighbor exchange, and third-nearest neighbor interactions for Fe magnetic moments are shown as J_1, J_2, and J_3, respectively.
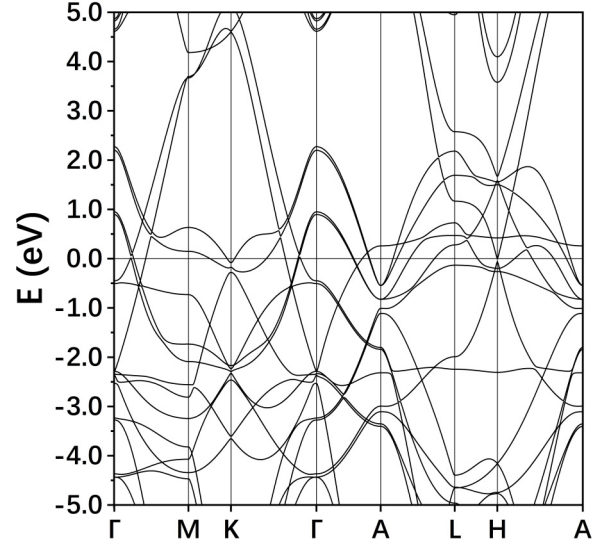

FIG. 6. The electronic structure of FeB_2 based on LSDA + SOC with (001) spin orientation.

Thus, the values of J_1 to J_4 can be evaluated by mapping the relative total energies of the five spin states and the obtained magnetic interactions are summarized inTable III. These four magnetic interactions are all ferromagnetic, in which J_1 and J_4 play a leading role. With the increase of U, the strength of these exchange parameters have somewhat differences, but the dominant terms do not change. Based on the spin exchange parameters in Table III, we calculate Curie temperatures by the mean-field theory (MFT) approximation [64] and MC simulations [47–49], which are also summarized in Table III. The calculated Curie temperature based on LSDA calculation is very high (1546 K) for MFT approximation, while the value from MC simulations is somewhat smaller (945 K). Meanwhile, the calculated Curie temperatures are not greatly affected by the value of U. In summary, FeB_4 is suggested to be a good candidate for potential high-temperature permanent magnet materials.
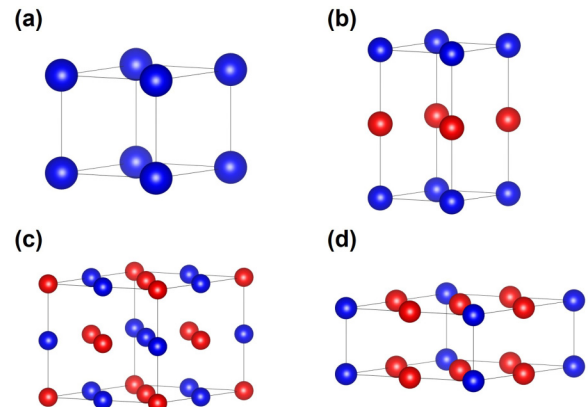

FIG. 7. The magnetic configurations of FeB_2 considered in DFT calculations. For clarity only Fe atoms are shown, while the blue and red ones represent Fe ions with up and down spin, respectively. (a)–(d) FM, AFM-1, AFM-2, and FIM-1 configurations, respectively.

TABLE V. Spin exchange parameters (in meV) of FeB_2 evaluated from LSDA $(+ U)$ calculations. Meanwhile, the calculated Curie temperature (in K) based on MFT and MC method with different values of U are also summarized in the table.

	Distance (Å)	LSDA	LSDA $+ U$ (= 0.5 eV)	LSDA $+ U$ (= 1.0 eV)	LSDA $+ U$ (= 1.5 eV)	LSDA $+ U$ (= 2.0 eV)
J_1	3.035	−2.16	−5.01	−11.49	−16.54	−26.52
J_2	3.045	−11.42	−16.17	−19.46	−23.17	−25.08
J_3	4.299	−1.81	−4.59	−6.70	−8.15	−8.21
T_C (MFT)		366	627	852	1044	1168
T_C (MC)		355	588	828	964	1054

B. FeB_2

FeB_2 crystallizes in the hexagonal structure (space group $P6/mmm$) [65] as shown in Fig. 5. Fe atoms occupy the $1a$ position: (0, 0, 0), and the site-symmetry group of Fe is (6/mmm), which also permits the E_1 and E_2 orbital multiplets allowing large MAE.

As one of the most important criterias of the permanent magnet, the magnetic moment on the Fe site is estimated to be 2.21 μ_B ($M_S = 0.0937$ $\mu_B/\text{Å}^3$) from LSDA calculations for FM configuration. Meanwhile, the MAE is calculated to be 5.394 MJ/m^3 with the easy-axis magnetization along the (001) direction by the energy differences approach, while based on the force theorem [42,43] the MAE is 5.688 MJ/m^3. The band structure from LSDA + SOC calculation with (001) spin direction is shown in Fig. 6. In a similar way to the FeB_4 case, we perform first-principles calculations for several different magnetic configurations of FeB_2, including

FM configuration, two AFM configurations, and one FIM configuration as shown in Fig. 7. As shown in Table IV, the FM configuration has the lowest total energy with different Hubbard U. The magnetic moments are comparable for different magnetic configurations with the same Hubbard U value (with a difference around ± 0.3 μ_B), suggesting that the energy-mapping method is an effective approach to roughly calculate interactions. As shown in Fig. 5, we consider four magnetic interactions labeled as J_1 to J_3. The total energies per unit cell for these four spin configurations are expressed as

$$E_{FM} = E_0 + J_1 + 3J_2 + 6J_3,$$
$$E_{AFM-1} = E_0 - J_1 + 3J_2 - 6J_3,$$
$$E_{AFM-2} = E_0 - J_1 - J_2 + 2J_3,$$
$$E_{FIM} = E_0 + J_1. \quad (2)$$

TABLE VI. Materials for permanent magnets by screening which have already been discussed in previous studies. Listed are the material's ICSD, formula, space group, the corresponding $3d$ translation elements and Wyckoff positions, the calculated MAE (MJ/m^3) from LSDA + SOC calculations and saturation magnetic moment M_s ($\mu_B/\text{Å}^3$) from LSDA calculations. The data in the previous theoretical and experimental work are also shown for comparison.

ICSD number	Material formula	Space group	Transition elements	Wyckoff positon	This work		Previous work			
							Experimental work		Theoretical work	
					MAE	Ms	MAE	Ms	MAE	Ms
150 640	FePt	123	Fe	$1a$	11.977	0.119			10.0 [51]	
53 259	Pt_2FeCu	123	Cu	$1a$	5.291	0.073			5.83 [32]	0.075 [32]
			Fe	$1c$						
42 564	Pt_2FeNi	123	Fe	$1a$	2.358	0.088			2.42 [32]	0.089 [32]
			Ni	$1c$						
102 620	CoPt	123	Co	$1a$	5.098	0.085	4.0 [66], 6.9 [67]		9.0 [68]	
634 628	MnGa	123	Mn	$1d$	2.256	0.092			2.0 [69]	0.087 [70]
181 719	FePd	123	Fe1	$1a$	1.833	0.118			1.28 [71]	0.114 [71]
			Fe2	$1c$					1.713 [72]	
180 896	FePd	123	Fe	$1a$	0.938	0.119	1.04 [72]		0.96 [72]	
76 636	$Fe_{16}N_2$	139	Fe1	$4d$	1.264	0.188	0.78 [52]		1.043 [54]	0.192[54]
			Fe2	$4e$						0.266 [53]
99 787	Fe_3Pt	139	Fe	$4e$	1.344	0.167			0.086 [73]	0.172 [73]
102 731	YCo_5	191	Co	$2c$	2.294	0.086	6.5 [74]		4.37 [56]	0.099[57], 0.096 [56]
52 972	Co_3Mn_2Ge	194	Mn	$4f$	1.465	0.147	1.18 [33]	0.087 [33]	1.44 [33]	0.147 [33]
633 778	Fe_2Ta	194	Fe	$2a$	2.023	0.062			1.25 [75]	0.059 [75]
643 689	$Mn_3V_2Si_3$	193	V	$4d$	0.798	0.078			0.85 [33]	0.063 [33]
625 559	YCo_3	194	Co1	$2a$	1.051	0.060	1.03 [76]	0.029 [76]		
			Co2	$2b$						
			Co3	$2c$						

Thus, the values of J_1 to J_3 can be evaluated by mapping the relative total energies of the four spin states and the obtained magnetic interactions are summarized in Table V. Based on the calculated spin exchange parameters from LSDA calculations, the Curie temperatures are estimated to be 366 K and 355 K using the MFT approximation [64] and MC method [47–49], respectively. With the increasing value of U, the Curie temperature by both the MFT approximation and MC method become higher as shown in Table V. According to its high saturation magnetization and large uniaxial MAE, FeB_2 is also suggested to be a good candidate for potential permanent magnet material.

V. CONCLUSION

In conclusion, we present a highly efficient search for permanent magnet candidates in the ICSD. Focusing on $3d$ materials where certain partially occupied orbital multiplets can significantly enhance the effect of SOC, we first screen $3d$ transition metal materials with potentially huge MAEs by simply checking whether the materials belong to the corresponding space groups and whether the $3d$ transition elements occupy the specific Wyckoff positions. Then first-principles high-throughput screening is performed based on the calculated saturation magnetic moment, magnetic anisotropy energy, and magnetic ground state. In addition to many materials discussed in earlier studies, finally five new candidates are proposed as potential permanent magnet materials. As examples, we present an investigation of detailed magnetic properties in FeB_4 and FeB_2, and discuss the effect of Coulomb interaction U on them. Our results show that $3d$ transition elements compounds may also have large MAE and we believe that these potential rare-earth-free permanent magnet materials deserve further experimental study.

TABLE VII. The space group, Wyckoff positions of Fe ions, and the calculated MAE (MJ/m^3) of Fe-B alloys in ICSD database (* materials for discussion in main text).

Formula	SG	Wyckoff position	MAE
FeB_2 [77]	62	$4c$	−0.0138
FeB_2 * [65]	191	$1a$	5.7143
FeB_4 [78]	58	$2a$	0.0935
FeB_4 [59]	58	$2b$	0.0074
FeB_4 [59]	64	$4a$	−0.0001
FeB_4 [59]	142	$8b$	0.0000
FeB_4 [59]	194	$2d$	−1.7967
FeB_4 * [59]	194	$2b, 2c$	2.4084
FeB_4 [59]	216	$4a$	−0.0018
FeB [79]	62	$4c$	−0.4758
FeB [77]	141	$8e$	0.3763
Fe_2B [80]	121	$8i$	−0.2615
Fe_2B [81]	140	$8h$	−0.3131
Fe_2B_7 [82]	55	$4h, 4g$	−0.1112
Fe_3B [83]	62	$4c$	−0.4710
Fe_3B [84]	82	$8g$	−0.1831
Fe_3B [83]	182	$6g$	0.1505
$Fe_{23}B_6$ [85]	225	$4a, 8c, 48h, 32f$	0.0001

APPENDIX

In the Appendix, we list these suggested permanent magnet materials which were already discussed in earlier studies in Table VI. Meanwhile, we also list the space groups, MAE, and Wyckoff positions occupied by Fe ions of Fe-B alloys existing in the ICSD database in Table VII.

[1] P. Campbell, *Permanent Magnet Materials and Their Application* (Cambridge University Press, Cambridge, England, 1996).

[2] R. Skomski and J. M. D. Coey, *Permanent Magnetism* (Routledge, Abingdon, England, 2019).

[3] J. M. D. Coey, *Rare-Earth Iron Permanent Magnets* (Oxford University Press, New York, 1996).

[4] J. F. Herbst, $R_2Fe_{14}B$ materials: Intrinsic properties and technological aspects, Rev. Mod. Phys. **63**, 819 (1991).

[5] D. Givord, H. S. Li, and J. M. Moreau, Magnetic properties and crystal structure of $Nd_2Fe_{14}B$, Solid State Commun. **50**, 497 (1984).

[6] D. Givord, H. S. Li, and R. Perrier de la Bâthie, Magnetic properties of $Y_2Fe_{14}B$ and $Nd_2Fe_{14}B$ single crystals, Solid State Commun. **51**, 857 (1984).

[7] K. H. J. Buschow, P. A. Naastepad, and F. F. Westendorp, Preparation of $SmCo_5$ permanent magnets, J. Appl. Phys. **40**, 4029 (1969).

[8] H. Zijlstra and F. F. Westendorp, Influence of hydrogen on the magnetic properties of $SmCo_5$, Solid State Commun. **7**, 857 (1969).

[9] J. M. D. Coey, Perspective and prospects for rare earth permanent magnets, Engineering **6**, 119 (2020).

[10] V. Ly, X. Wu, L. Smillie, T. Shoji, A. Kato, A. Manabe, and K. Suzuki, Low-temperature phase MnBi compound: A potential candidate for rare-earth free permanent magnets, J. Alloys Compd. **615**, S285 (2014).

[11] M. D. Kuz'min, K. P. Skokov, H. Jian, I. Radulov, and O. Gutfleisch, Towards high-performance permanent magnets without rare earths, J. Phys.: Condens. Matter **26**, 064205 (2014).

[12] M. Werwiński, S. Kontos, K. Gunnarsson, P. Svedlindh, J. Cedervall, V. Höglin, M. Sahlberg, A. Edström, O. Eriksson, and J. Rusz, Magnetic properties of Fe_5SiB_2 and its alloys with P, S, and Co, Phys. Rev. B **93**, 174412 (2016).

[13] V. Shtender, D. Hedlund, S. R. Larsen, P. Svedlindh, and M. Sahlberg, Structural and magnetic properties of new members of the 3:29 phase from the Ce–Fe–Mn system and 1:11 from the Ce–Co–Mn, J. Alloys Compd. **855**, 157435 (2021).

[14] B. Balamurugan, B. Das, W. Y. Zhang, R. Skomski, and D. J. Sellmyer, Hf–Co and Zr–Co alloys for rare-earth-free permanent magnets, J. Phys.: Condens. Matter **26**, 064204 (2014).

[15] M. Yue, X. Zhang, and J. P. Liu, Fabrication of bulk nanostructured permanent magnets with high energy density: Challenges and approaches, Nanoscale **9**, 3674 (2017).

[16] B. Balasubramanian, B. Das, R. Skomski, W. Y. Zhang, and D. J. Sellmyer, Novel nanostructured rare-earth-free magnetic materials with high energy products, Adv. Mater. **25**, 6090 (2013).

[17] F. M. Abel, V. Tzitzios, E. Devlin, S. Alhassan, D. J. Sellmyer, and G. C. Hadjipanayis, Enhancing the ordering and coercivity of L_{10}FePt nanostructures with bismuth additives for applications ranging from permanent magnets to catalysts, ACS Appl. Nano Mater. **2**, 3146 (2019).

[18] E. Anagnostopoulou, B. Grindi, L. M. Lacroix, F. Ott, I. Panagiotopoulos, and G. Viau, Dense arrays of cobalt nanorods as rare-earth free permanent magnets, Nanoscale **8**, 4020 (2016).

[19] S. Ener, E. Anagnostopoulou, I. Dirba, L.-M. Lacroix, F. Ott, T. Blon, J.-Y. Piquemal, K. P. Skokov, O. Gutfleisch, and G. Viau, Consolidation of cobalt nanorods: A new route for rare-earth free nanostructured permanent magnets, Acta Mater. **145**, 290 (2018).

[20] T. J. Nummy, S. P. Bennett, T. Cardinal, and D. Heiman, Large coercivity in nanostructured rare-earth-free Mn_xGa films, Appl. Phys. Lett. **99**, 252506 (2011).

[21] T. R. Gao, Y. Q. Wu, S. Fackler, I. Kierzewski, Y. Zhang, A. Mehta, M. J. Kramer, and I. Takeuchi1, Combinatorial exploration of rare-earth-free permanent magnets: Magnetic and microstructural properties of Fe-Co-W thin films, Appl. Phys. Lett. **102**, 022419 (2013).

[22] H. Sepehri-Amin, Y. Tamazawa, M. Kambayashi, G. Saito, Y. K. Takahashi, D. Ogawa, T. Ohkubo, S. Hirosawa, M. Doi, T. Shima, and K. Hono, Achievement of high coercivity in $Sm(Fe_{0.8}Co_{0.2})_{12}$ anisotropic magnetic thin film by boron doping, Acta Mater. **194**, 337 (2020).

[23] T. Zhang, Y. Jiang, Z. Song, H. Huang, Y. He, Z. Fang, H. Weng, and C. Fang, Catalogue of topological electronic materials, Nature (London) **566**, 475 (2019).

[24] M. G. Vergniory, L. Elcoro, C. Felser, N. Regnault, B. A. Bernevig, and Z. Wang, A complete catalogue of high-quality topological materials, Nature (London) **566**, 480 (2019).

[25] F. Tang, H. C. Po, A. Vishwanath, and X. G. Wan, Comprehensive search for topological materials using symmetry indicators, Nature (London) **566**, 486 (2019).

[26] M. Z. Hasan and C. L. Kane, *Colloquium:* Topological insulators, Rev. Mod. Phys. **82**, 3045 (2010).

[27] V. I. Anisimov, F. Aryasetiawan, and A. I. Lichtenstein, First-principles calculations of the electronic structure and spectra of strongly correlated systems: The LDA+U method, J. Phys.: Condens. Matter **9**, 767 (1997).

[28] X. Wan, A. M. Turner, A. Vishwanath, and S. Y. Savrasov, Topological semimetal and fermi-arc surface states in the electronic structure of pyrochlore iridates, Phys. Rev. B **83**, 205101 (2011).

[29] X. Wan, A. Vishwanath, and S. Y. Savrasov, Computational Design of Axion Insulators Based on 5d Spinel Compounds, Phys. Rev. Lett. **108**, 146601 (2012).

[30] Y. Xu, L. Elcoro, Z. Song, B. J. Wieder, M. G. Vergniory, N. Regnault, Y. Chen, C. Felser, and B. Andrei Bernevig, High-throughput calculations of magnetic topological materials, Nature (London) **586**, 702 (2020).

[31] A. G. Kusne, T. Gao, A. Mehta, L. Ke, M. C. Nguyen, K. M. Ho, V. Antropov, C. Z. Wang, M. J. Kramer, C. Long, and I. Takeuchi, On-the-fly machine-learning for high-throughput experiments: Search for rare-earth-free permanent magnets, Sci. Rep. **4**, 6367 (2014).

[32] A. Vishina, O. Y. Vekilova, T. Björkman, A. Bergman, H. C. Herper, and O. Eriksson, High-throughput and data-mining approach to predict new rare-earth free permanent magnets, Phys. Rev. B **101**, 094407 (2020).

[33] A. Vishina, D. Hedlund, V. Shtender, E. K. Delczeg-Czirjak, S. R. Larsen, O. Y. Vekilova, S. Huang, L. Vitos, P. Svedlindh, M. Sahlberg, O. Eriksson, and H. C.Herpera, Data-driven design of a new class of rare-earth free permanent magnets, Acta Mater. **212**, 116913 (2021).

[34] A. Kovacs, J. Fischbacher, M. Gusenbauer, H. Oezelt, H. C. Herper, O. Y. Vekilova, P. Nieves, S. Arapan, and T. Schrefl, Computational design of rare-earth reduced permanent magnets, Engineering **6**, 148 (2020).

[35] P. Nieves, S. Arapan, J. Maudes-Raedo, R. Marticorena-Sánchez, N. L. Del Brío, A. Kovacs, C. Echevarria-Bonet, D. Salazar, J. Weischenberg, H. Zhang, O. Y. Vekilova, R. Serrano-López, J. M. Barandiaran, K. Skokov, O. Gutfleisch, O. Eriksson, H. C. Herper, T. Schrefl, and S. Cuesta-López, Database of novel magnetic materials for high-performance permanent magnet development, Comput. Mater. Sci. **168**, 188 (2019).

[36] R. Allmann and R. Hinek, The introduction of structure types into the Inorganic Crystal Structure Database ICSD, Acta Crystallogr. A **63**, 412 (2007).

[37] J. Li, Q. Yao, L. Wu, Z. Hu, B. Gao, X. G. Wan, and Q. H. Liu, Designing light-element materials with large effective spin-orbit coupling, Nat. Commun. **13**, 919 (2022).

[38] D. Khomskii, *Transition Metal Compounds* (Cambridge University Press, Cambridge, England, 2014).

[39] M. Imada, A. Fujimori, and Y. Tokura, Metal-insulator transitions, Rev. Mod. Phys. **70**, 1039 (1998).

[40] F. Tang and X. Wan, Exhaustive construction of effective models in 1651 magnetic space groups, Phys. Rev. B **104**, 085137 (2021).

[41] D. Wang, F. Tang, Y. Du, and X. Wan, First-principles study of the giant magnetic anisotropy energy in bulk Na_4IrO_4, Phys. Rev. B **96**, 205159 (2017).

[42] A. R. Mackintosh and O. K. Andersen, *Electrons at the Fermi Surface* (Cambridge Univeristy Press, Cambridge, England, 1980).

[43] M. Weinert, R. E. Watson, and J. W. Davenport, Total-energy differences and eigenvalue sums, Phys. Rev. B **32**, 2115 (1985).

[44] P. Blaha, K. Schwarz, G. Madsen, D. Kvasnicka, and J. Luitz, *WIEN2k, An augmented plane wave+ Local Orbitals Program for Calculating Crystal Properties*, edited by K. Schwarz (Vienna University of Technology, Austria, 2001).

[45] S. H. Vosko, L. Wilk, and M. Nusair, Accurate spin-dependent electron liquid correlation energies for local spin density

calculations: A critical analysis, Can. J. Phys. **58**, 1200 (1980).

[46] D. D. Koelling and B. N. Harmon, A technique for relativistic spin-polarised calculations, J. Phys. C: Solid State Phys. **10**, 3107 (1977).

[47] N. Metropolis and S. Ulam, The monte carlo method, J. Am. Stat. Assoc. **44**, 335 (1949).

[48] Z.-X. Shen, C. Su, and L. He, High-throughput computation and structure prototype analysis for two-dimensional ferromagnetic materials, NPJ Comput. Mater. **8**, 132 (2022).

[49] K. Cao, G.-C. Guo, D. Vanderbilt, and L. He, First-Principles Modeling of Multiferroic RMn$_2$O$_5$, Phys. Rev. Lett. **103**, 257201 (2009).

[50] R. F. C. Farrow, D. Weller, R. F. Marks, M. F. Toney, and A. Cebollada, Control of the axis of chemical ordering and magnetic anisotropy in epitaxial FePt films, J. Appl. Phys. **79**, 5967 (1996).

[51] J. U. Thiele, L. Folks, M. F. Toney, and D. K. Weller, Perpendicular magnetic anisotropy and magnetic domain structure in sputtered epitaxial FePt (001) L1$_0$ films, J. Appl. Phys. **84**, 5686 (1998).

[52] H. Takahashi, K. Mitsuoka, M. Komuro, and Y. Sugita, Ferromagnetic resonance studies of Fe$_{16}$N$_2$ films with a giant magnetic moment, J. Appl. Phys. **73**, 6060 (1993).

[53] N. Ji, V. Lauter, X. Zhang, H. Ambaye, and J. P. Wang, Strain induced giant magnetism in epitaxial Fe$_{16}$N$_2$ thin film, Appl. Phys. Lett. **102**, 072411 (2013).

[54] W. Zhou, L. Liu, and P. Wu, Effect of biaxial strain on the magnetism of Fe$_{16}$N$_2$: Density-functional investigations, Phys. Lett. A **378**, 909 (2014).

[55] J. Wang, Environment-friendly bulk Fe$_{16}$N$_2$ permanent magnet: Review and prospective, J. Magn. Magn. Mater. **497**, 165962 (2020).

[56] M. Matsumoto, R. Banerjee, and J. B. Staunton, Improvement of magnetic hardness at finite temperatures: Ab initio disordered local-moment approach for YCo$_5$, Phys. Rev. B **90**, 054421 (2014).

[57] J. M. Alameda, D. Givord, R. Lemaire, and Q. Lu, Co energy and magnetization anisotropies in RCo$_5$ intermetallics between 4.2 K and 300 K, J. Appl. Phys. **52**, 2079 (1981).

[58] G. Hoffer and K. Strnat, Magnetocrystalline anisotropy of YCo$_5$ and Y$_2$Co$_{17}$, IEEE Trans. Magn. **2**, 487 (1966).

[59] X. Jiang and J. Zhao, Evolution of boron clusters in iron tetraborides under high pressure: Semiconducting and ferromagnetic superhard materials, RSC Adv. **5**, 48012 (2015).

[60] K. Ikeda, T. Nakamichi, T. Yamada, and M. Yamamoto, Ferromagnetism in Fe$_2$Sc with the hexagonal MgZN$_2$-type structure, J. Phys. Soc. Jpn. **36**, 611 (1974).

[61] B. Li, H. Sun, and C. Chen, First-principles calculation of the indentation strength of FeB$_4$, Phys. Rev. B **90**, 014106 (2014).

[62] C. de Graaf and B. Ria, *Magnetic Interactions in Molecules and Solids* (Springer, New York, 2016).

[63] H. Xiang, C. Lee, H. -J. Koo, X. Gong, and M. -H. Whangbo, Magnetic properties and energy-mapping analysis, Dalton Trans. **42**, 823 (2013).

[64] J. S. Smart, *Effective Field Theories of Magnetism* (Saunders, Philadelphia, 1966).

[65] L. G. Voroshnin, L. S. Lyakhovich, G. G. Panich, and G. F. Protasevich, The structure of Fe-B alloys, Met. Sci. Heat Treat. **12**, 732 (1970).

[66] P. Eurin and J. Pauleve, Influence of thermomagnetic treatments on the magnetic properties of Co-Pt 50-50 alloy, IEEE Trans. Magn. **5**, 216 (1969).

[67] I. V. Solovyev, P. H. Dederichs, and I. Mertig, Origin of orbital magnetization and magnetocrystalline anisotropy in TX ordered alloys (where T= Fe and Co and X= Pd and Pt), Phys. Rev. B **52**, 13419 (1995).

[68] A. Sakuma, First principle calculation of the magnetocrystalline anisotropy energy of fept and copt ordered alloys, J. Phys. Soc. Jpn. **63**, 3053 (1994).

[69] S. Mizukami, F. Wu, A. Sakuma, J. Walowski, D. Watanabe, T. Kubota, X. Zhang, H. Naganuma, M. Oogane, Y. Ando, and T. Miyazaki, Long-Lived Ultrafast Spin Precession in Manganese Alloys Films with a Large Perpendicular Magnetic Anisotropy, Phys. Rev. Lett. **106**, 117201 (2011).

[70] A. Sakuma, Electronic structures and magnetism of CuAu-type MnNi and MnGa, J. Magn. Magn. Mater. **187**, 105 (1998).

[71] R. Pathak, O. A. Golovnia, E. G. Gerasimov, A. G. Popov, N. I. Vlasova, R. Skomski, and A. Kashyap, Ab initio study of the magnetic properties of possible phases in binary Fe-Pd alloys, J. Magn. Magn. Mater. **499**, 166266 (2020).

[72] I. Galanakis, M. Alouani, and H. Dreyssé, Perpendicular magnetic anisotropy of binary alloys: A total-energy calculation, Phys. Rev. B **62**, 6475 (2000).

[73] H. Suzuki, K. Nakamura, T. Akiyama, and T. Ito, Magnetic structures and magnetocrystalline anisotropy in bulk and thin film Fe$_3$Pt, Appl. Surf. Sci. **254**, 7843 (2008).

[74] J. M. D. Coey, Permanent magnets: Plugging the gap, Scr. Mater. **67**, 524 (2012).

[75] A. Edström, Magnetocrystalline anisotropy of laves phase Fe$_2$Ta$_{1-x}$W$_x$ from first principles: Effect of $3d-5d$ hybridization, Phys. Rev. B **96**, 064422 (2017).

[76] D. S. Neznakhin, A. M. Bartashevich, A. S. Volegov, M. I. Bartashevich, and A. V. Andreev, Magnetic anisotropy in RCo$_3$ (r = lu and y) single crystals, J. Magn. Magn. Mater. **539**, 168367 (2021).

[77] A. N. Kolmogorov, S. Shah, E. R. Margine, A. F. Bialon, T. Hammerschmidt, and R. Drautz, New Superconducting and Semiconducting Fe-B Compounds Predicted with an *Ab Initio* Evolutionary Search, Phys. Rev. Lett. **105**, 217003 (2010).

[78] E. Bykova, Single-crystal X-ray diffraction at extreme conditions in mineral physics and material sciences, Ph.D. thesis, Universitaet of Bayreuth (Germany), 2015.

[79] T. Bjurström, *Röntgenanalyse der systeme eisen-bor, kobalt-bor und nickel-bor* (Almqvist & Wiksell, Bonn, Germany, 1933).

[80] F. Wever and A. Müller, Über das Zweistoffsystem Eisen-Bor und über die Struktur des Eisenborides Fe$_4$B$_2$, Z. Anorg. Allg. Chem. **192**, 317 (1930).

[81] C. Kapfenberger, B. Albert, R. Pöttgen, and H. Huppertz, Structure refinements of iron borides Fe$_2$B and FeB, Z. Kristallogr. Cryst. Mater. **221**, 477 (2006).

[82] E. Bykova, H. Gou, M. Bykov, M. Hanfland, L. Dubrovinsky, and N. Dubrovinskaia, Crystal structures and compressibility of novel iron borides Fe$_2$B$_7$ and Fe$_x$B$_{50}$ synthesized at high pressure and high temperature, J. Solid State Chem. **230**, 102 (2015).

[83] W. H. Zhang, Z. Q. Lv, Z. P. Shi, S. H. Sun, Z. H. Wang, and W. T. Fu, Electronic, magnetic and elastic properties of ε-phases Fe$_3$X(X = B, C, N) from density-functional

theory calculations, J. Magn. Magn. Mater. **324**, 2271 (2012).

[84] W. K. Wang, H. Iwasaki, and K. Fukamichi, Effect of high pressure on the crystallization of an amorphous $Fe_{83}B_{17}$ alloy, J. Mater. Sci. **15**, 2701 (1980).

[85] B. Idzikowski, J.-M. Szajek, A. Greneche, and J. Kovaā, Nanogranular $Fe_xNi_{23-x}B_6$ phase formation during devitrificationof nickel-rich $Ni_{64}Fe_{16}Zr_7B_{12}Au_1$ amorphous alloy, Appl. Phys. Lett. **85**, 1392 (2004).